

Figure 1.4.5: Pairing rotational band associated with the ground states of the Sn-isotopes. The lines represent the energies calculated according to the expression $BE = B(^{50+N}\text{Sn}_N) - 8.124N + 46.33$ (Brink, D. and Broglia (2005)), subtracting the contribution of the single nucleon addition to the nuclear binding energy obtained by a linear fitting of the binding energies of the whole Sn chain. The estimate of $\hbar^2/2I$ was obtained using the single j -shell model (see, e.g., Brink, D. and Broglia (2005), Appendix H). The numbers given on the abscissa are the absolute value of the experimental $gs \rightarrow gs$ cross section (in units of μb). (After Potel, G. et al. (2013)).

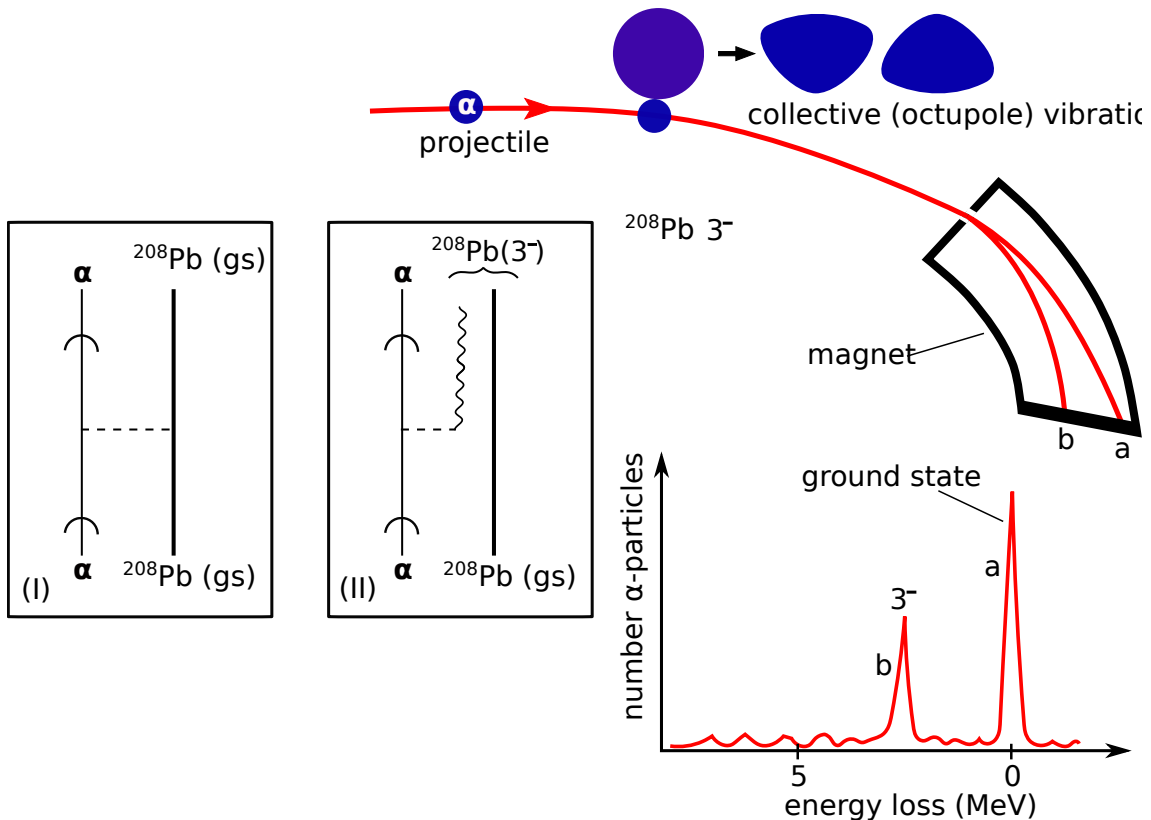


Figure 2.1.1: (color online) Schematic representation of: **elastic** a (population of the ground state), and **inelastic** b (population lowest octupole vibration at 2.62 MeV) processes associated with the reaction $^{208}\text{Pb}(\alpha, \alpha')^{208}\text{Pb}^*$ (for more details see Sect. 2.3 and App. 2.A). In the inset (I) a schematic Nuclear Field Theory (reaction plus structure) (NFT(r+s)) diagram describing the elastic process (potential scattering, dashed horizontal line) is displayed (see e.g. Broglia et al. (2016) and refs. therein). The α -projectile moving in the continuum is represented by an arrowed (curved) line. From the measurement of the elastic differential cross section one can deduce the partial wave phase shifts (Appendix 2.C). In the inset (II) a schematic NFT(r+s) diagram describing the inelastic excitation (see Fig. 2.C.1) of the low-lying octupole vibration (wavy line) of ^{208}Pb by the action of the transient field created by the α -particle on the target (horizontal dashed line) is given (see App. 2.A). Outgoing α particles are deflected in a spectograph and recorded in a detector. The corresponding excitation function is given in the lowest part of the figure (after Mottelson (1976b)).

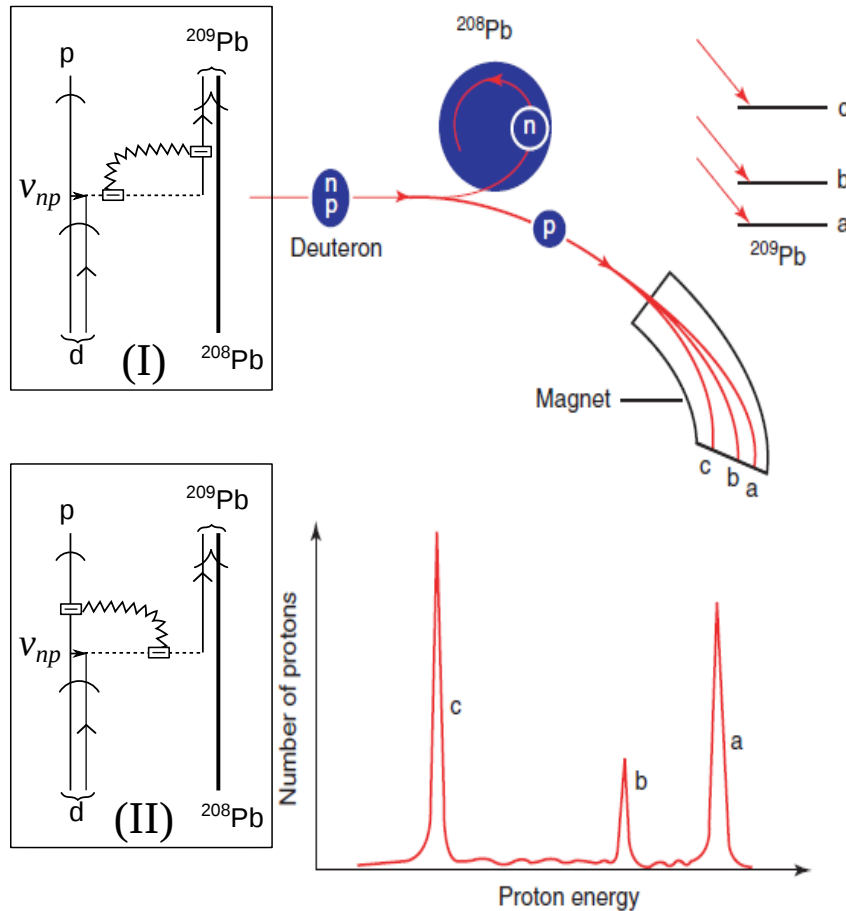


Figure 2.1.2: (Color online) Schematic representation of the one-nucleon transfer reaction $^{208}\text{Pb}(d, p)^{209}\text{Pb}$ populating valence single-particle states of ^{209}Pb . In the inset a schematic NFT($r+s$) diagram describing the process is shown. Curved arrowed lines describe the projectile d (deuteron) and outgoing particle p (proton) moving in the continuum. The short horizontal arrowed line labeled v_{np} represents the proton–neutron interaction inducing the transfer process (dashed horizontal line) while the open dashed rectangle indicates the Particle Recoil Coupling (PRC) vertex. That is, the coupling of the relative motion to the recoil process described in terms of a jagged line (App. 2.C). This information is carried out in the center of mass system by the outgoing particles in the final channel. Within this context the jagged line is involved in a virtual process (insets (I) and (II)). The energy and momentum of the outgoing proton reflects the recoil, the Q -value of the reaction and the excitation energy of the final state as analyzed in the magnet and recorded in the particle detector (a,b,c) (after Mottelson (1976b)).

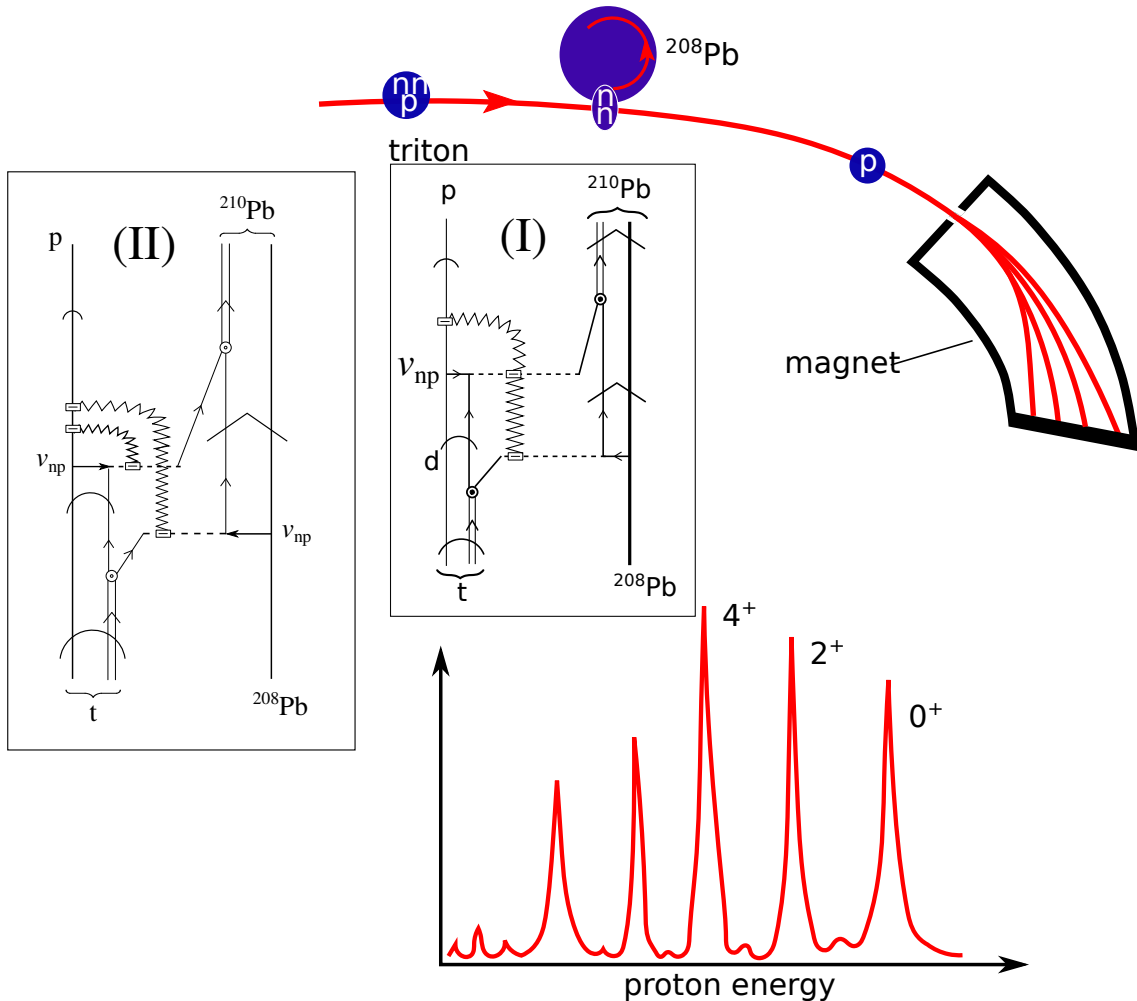


Figure 2.1.3: (Color online) Schematic representation of the two–nucleon transfer reaction $^{208}\text{Pb}(t, p)^{210}\text{Pb}$ process populating the ground state 0^+ , and two particle excited states 2^+ and 4^+ . That is, monopole, quadrupole and hexadecapole pair addition modes (multipole pairing vibrations) of ^{208}Pb (App. 7.F; see also Brink, D. and Broglia (2005) Sect. 5.3.1 p. 108). In the inset (I) a $\text{NFT}(r+s)$ diagram of the (successive) transfer process is displayed. The jagged line brings information to the outgoing nuclei in the exit channel (CM system), of the change in scaling in the asymptotic outgoing waves with respect to the incoming ones, concerning the different mass partitions (recoil) of summed value $2m$ (App. 2.C; concerning the apparent non–linearity that is the direct coupling of two recoil modes, this can be avoided drawing the process as shown in inset (II); see also Sect. 2.B.3; see also Fig. 2.7.10), this information is carried out to the detector by the outgoing proton (see App. 2.B, Sect. 2.B.3) (after Mottelson (1976b)).

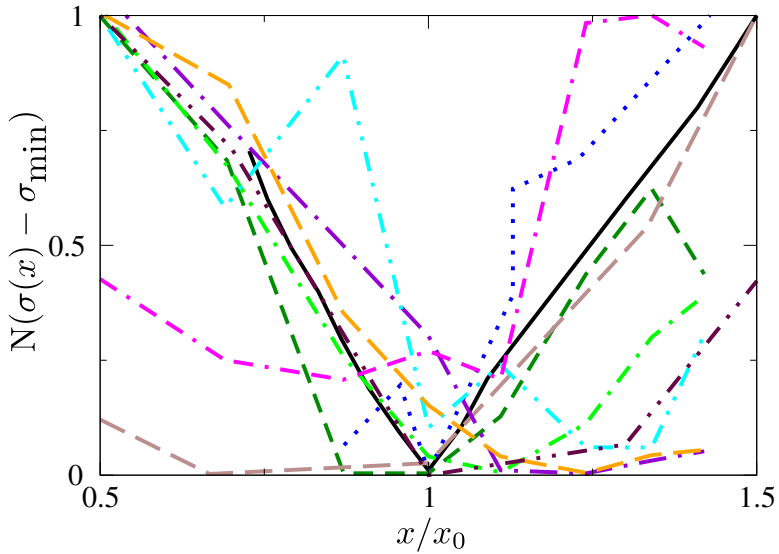


Figure 2.4.1: (Color online) Root mean square deviations $\sigma(x)$ (see Table 2.4.1) between theoretical predictions and experimental values of the different structural properties which “completely” characterize the open-shell nucleus ^{120}Sn (Idini et al. (2015)). After Broglia et al. (2016).

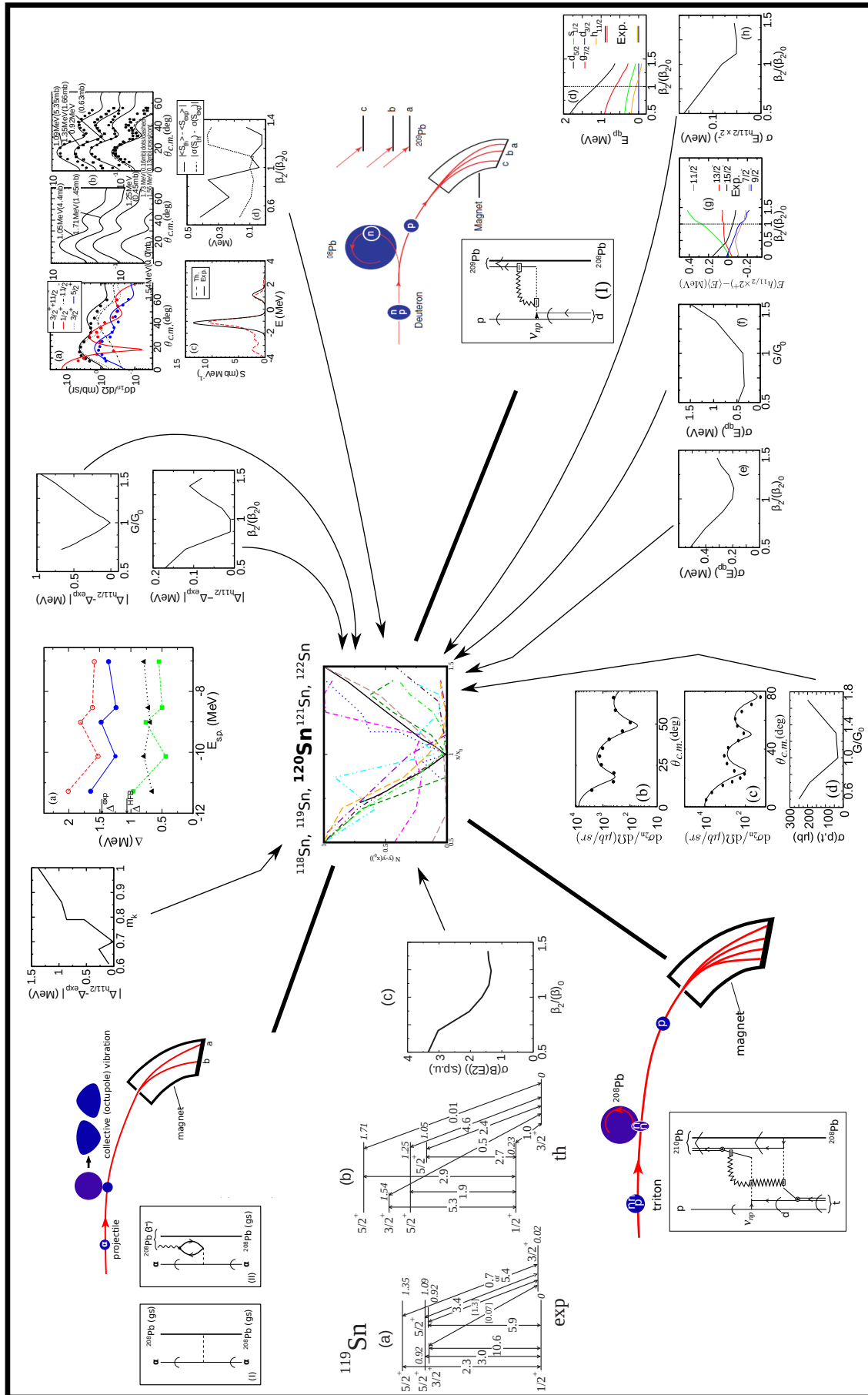
the variety of dressed (renormalized) elementary modes of excitation of the nucleus under study. In particular, diagrams **(b)**, **(c)** of Fig 2.4.2 describe inelastic and two-nucleon transfer processes while diagrams **(d)**–**(f)** portray one-nucleon transfer reactions.

In all orders in the particle vibration coupling vertex ((PVC), solid dot), starting from second order (graph (f)), NFT diagrams take care of the Pauli principle acting between the quasiparticles considered explicitly (continuous curves) and those participating in the modes (double wavy lines), as well as between modes. As a consequence, self energy processes based on pure or little collective two quasiparticle excitations are screened out or eliminated.

2.5 Non-orthogonality

Let us now consider a system based on a closed shell nucleus, namely two protons moving around ^{208}Pb . The ground state of $^{210}_{84}\text{Po}_{126}$ can be viewed as the proton pair addition mode of the doubly closed shell nucleus $^{208}_{82}\text{Pb}_{126}$, mode displaying $J^\pi = 0^+$ and $\beta = +2$ (transfer-) quantum numbers. Within this framework $^{209}_{83}\text{Bi}_{126}$ is expected to be a *bona fide* proton single-particle system ($\beta = +1$), in which the $g_{7/2}, d_{5/2}, h_{11/2}, d_{3/2}$ and $s_{1/2}$ valence orbitals are occupied, the odd proton occupying, in the ground state, a substate of the $h_{9/2}$ orbital.

This picture can be specifically probed through one-proton stripping and pick


 Figure 2.10.1: Characterization of ^{120}Sn .

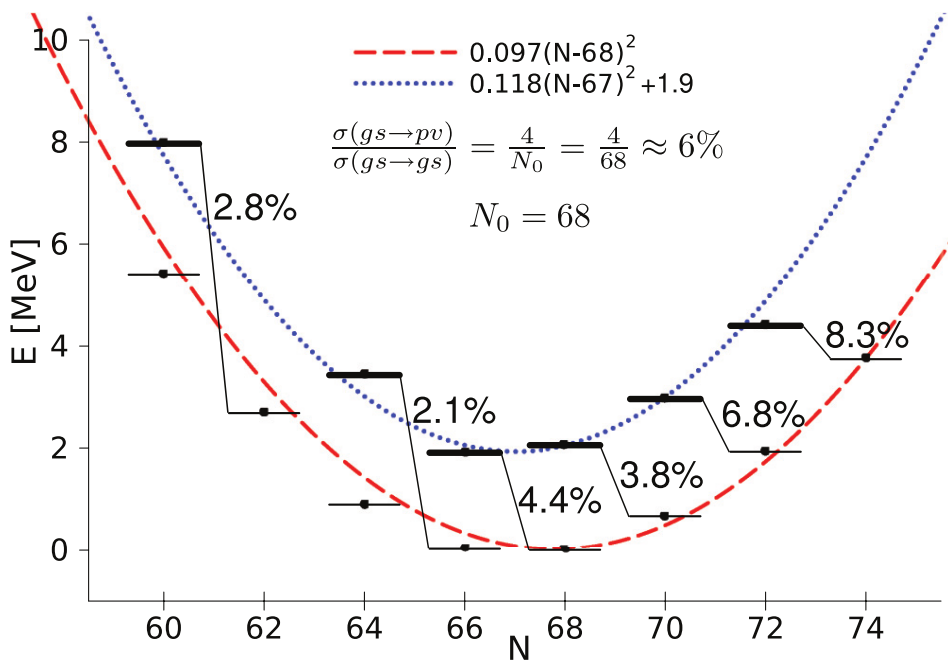


Figure 3.1.4: The weighted average energies ($E_{exc} = \sum_i E_i \sigma_i / \sum_i \sigma_i$) of the excited 0^+ states below 3 MeV in the Sn isotopic chain are shown on top of the pairing rotational band, already displayed in Fig. 3.1.3. Also indicated is the percentage of cross section for two-neutron transfer to excited states, normalized to the cross sections populating the ground states (after Potel, G. et al. (2013b)). The estimate of the ratio of cross sections displayed on top of the figure was obtained making use of the single j -shell model (see Eq. (4.2.3); see also Brink, D. and Broglia (2005) and references therein).

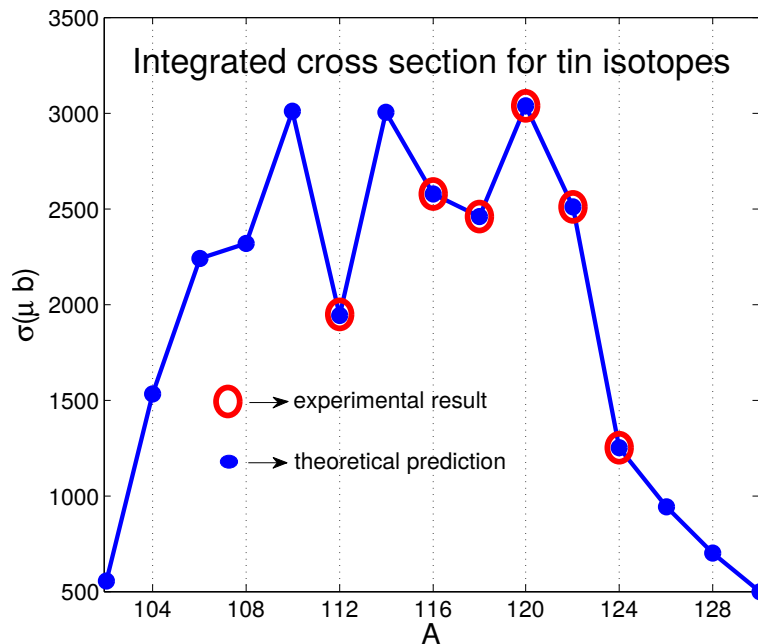


Figure 3.1.6: Absolute value of the two-nucleon transfer cross section $^{A+2}\text{Sn}(p, t)^A\text{Sn}(\text{gs})$ ($A = 112, 116, 118, 120, 122, 124$ cf. Potel, G. et al. (2013a) Potel, G. et al. (2013b)) calculated taking into account successive and simultaneous transfer in second order DWBA, properly corrected for non-orthogonality contributions in comparison with the experimental data (Guazzoni, P. et al. (1999), Guazzoni, P. et al. (2004), Guazzoni, P. et al. (2006), Guazzoni, P. et al. (2008), Guazzoni, P. et al. (2011), Guazzoni, P. et al. (2012)).

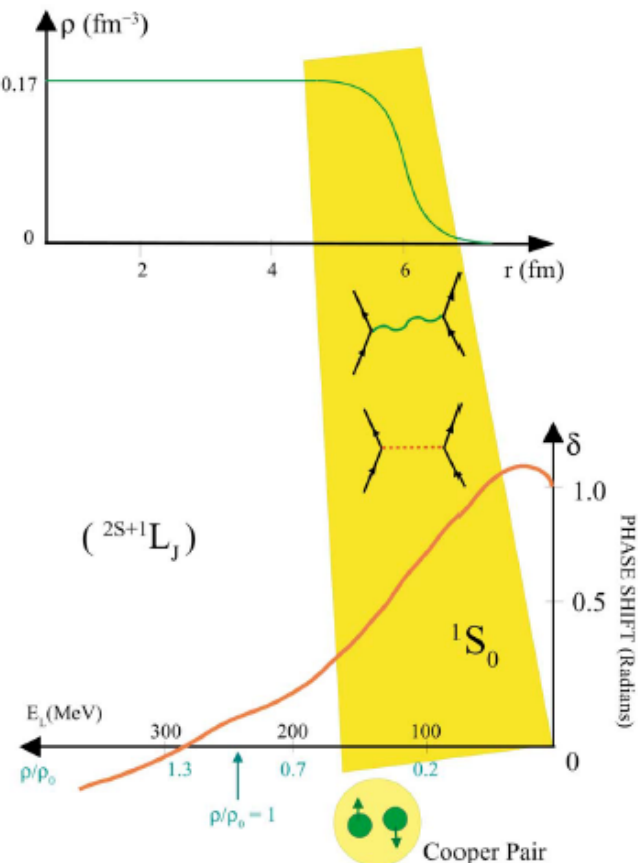


Figure 3.6.1: (top) Nuclear density ρ in units of fm^{-3} , plotted as a function of the distance r (in units of fm) from the centre of a nucleus lying along the stability valley (for comparison with a bound unstable nucleus lying at the neutron drip line see Fig. 4.2.2). Saturation density correspond to $\approx 0.17 \text{ fm}^{-3}$, equivalent to $2.8 \times 10^{14} \text{ g/cm}^3$ (after Bohr and Mottelson (1969)). Because of the short range of the nuclear force, the strong force, the nuclear density changes from 90% of saturation density to 10% within 0.65 fm, i.e. within the nuclear diffusivity. (bottom) Phase shift parameter associated with the elastic scattering of two nucleons moving in states of time reversal, so called 1S_0 phase shift, in keeping with the fact that the system is in a singlet state of spin zero. The solution of the Schrödinger equation describing the elastic scattering of a nucleon from a scattering centre (in this case another nucleon) is, at large distances from the scattering centre a superposition of the incoming wave and of the outgoing, scattering wave. The interaction of the incoming particle with the target particle changes only the amplitude of the outgoing wave. This amplitude can be written in terms of a real phase shift or scattering phase δ . Positive values of δ implies an attractive interaction, negative a repulsive one. For low relative velocities (kinetic energies E_L), i.e. around the nuclear surface where the density is low, the 1S_0 phase shift arising from the exchange of mesons (e.g. pions, represented by an horizontal dotted line) between nucleons (represented by upward pointing arrowed lines) is attractive. This mechanism provides about half of the glue to nucleons moving in time reversal states to form Cooper pairs. These pairs behaves like quasi-bosons and eventually condense (Fig. 3.3.5) in a single quantal state leading to nuclear superfluidity. Cooper pair formation is further assisted by the exchange of collective surface vibrations (wavy curve in the scattering process) between the members of the pair (after Broglia, R. A. (2002)).

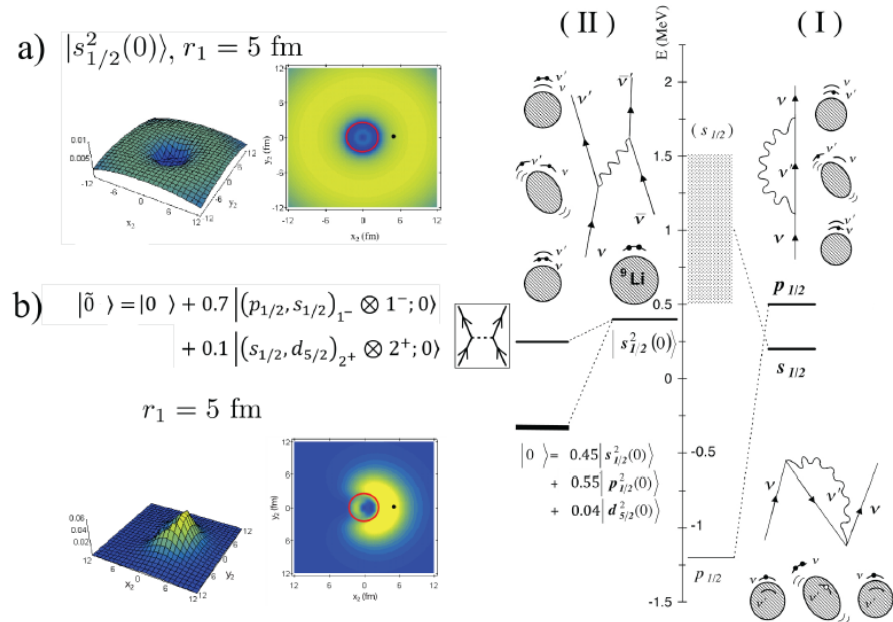


Figure 3.6.3: (Color online) In (I) and (II) the NFT processes renormalizing the single-particle motion (${}^{10}\text{Li}$) and leading to the effective interaction, sum of the bare (horizontal dotted lines) and induced (wavy curves) interactions which bind the two-neutron halo to the core of ${}^9\text{Li}$ thus leading to the $|{}^{11}\text{Li}\rangle$ ground state are displayed. In a) and b) are also displayed the spatial structure of the pure $|s_{1/2}^2(0)\rangle$ configuration and that of the two-neutron halo $|\tilde{0}\rangle$ Cooper pair. The modulus squared wave function $|\Psi_0(\mathbf{r}_1, \mathbf{r}_2)|^2 = |\langle \mathbf{r}_1, \mathbf{r}_1 | 0^+ \rangle|^2$ describing the motion of the two halo neutrons around the ${}^9\text{Li}$ core is shown as a function of the cartesian coordinates of particle 2, for fixed values of the position of particle 1 ($r_1 = 5 \text{ fm}$) represented by a solid dot, while the core ${}^9\text{Li}$ is shown as a red circle. The numbers appearing on the z -axis of the three-dimensional plots displayed on the left side of the figure are in units of fm^{-2} . After Barranco, F. et al. (2001).

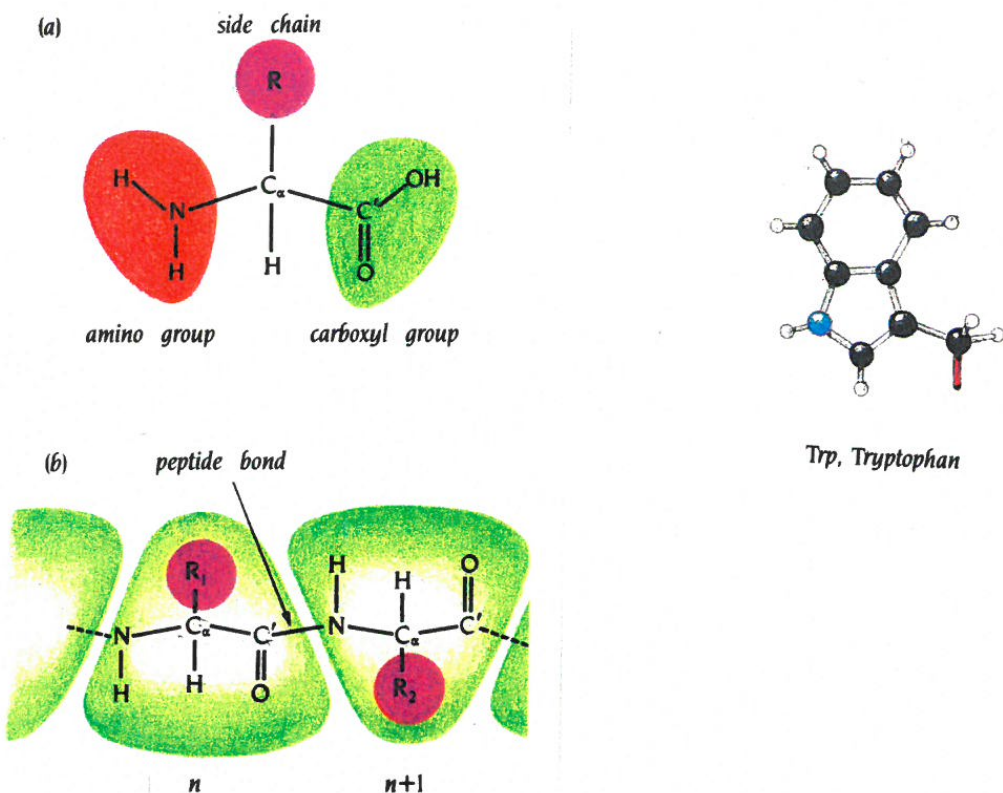


Figure 3.D.5: (Color online) Proteins are built up by amino acids that are linked by peptide bonds into a polypeptide chain. (a) Schematic diagram of an amino acid. A central carbon atom C_α is attached to an amino group, NH_2 , a carboxyl group $C'OOH$, a hydrogen atom H, and a side chain, R. (b) In a polypeptide chain the carboxyl group of amino acid has formed a peptide bond C–N, to the amino group of amino acid $n+1$. One water molecule is eliminated in this process. The repeating units, which are called residues, are divided into main-chain atoms and side chains. The main-chain part, which is identical in all residues, contains a central C_α atom attached to an NH group, a $C'=O$ group, and an H atom. The side-chain R, which is different for different residues is bound to the C_α atom. In the upper right, an example of side chain associated with the amino acid Tryptophan, also denoted Trp or W. Black spheres stand for carbon atoms (C), blue for nitrogen (N). Small, white spheres stand for hydrogen (H) (After Branden and Tooze (1991)).

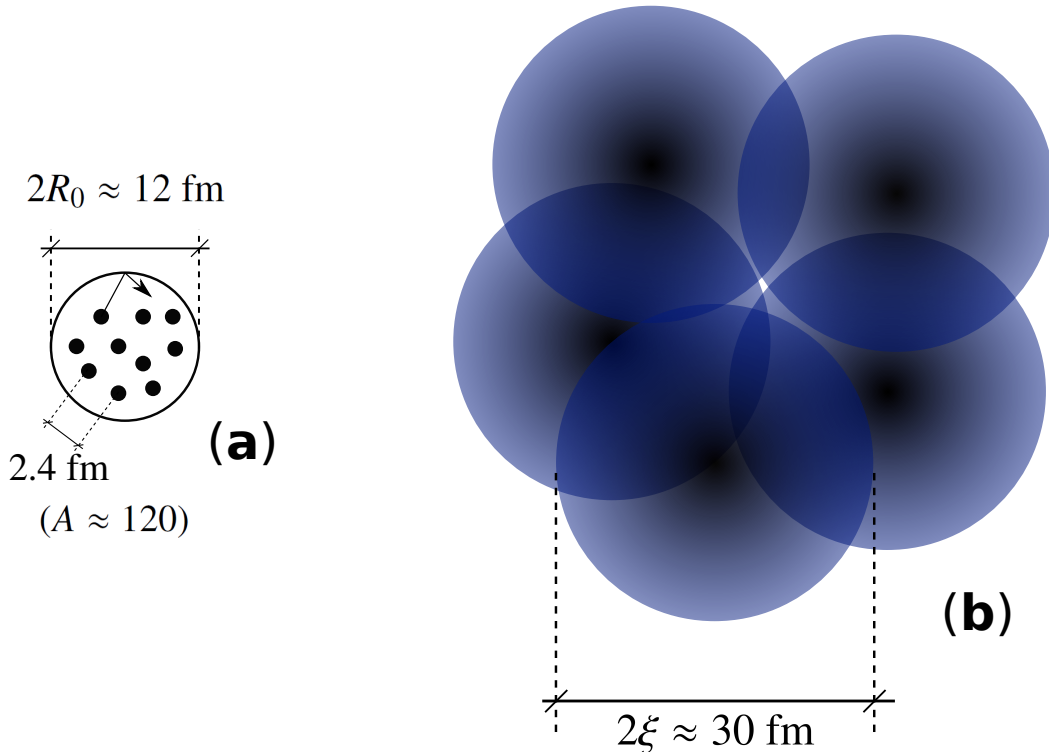


Figure 4.2.1: (a) Schematic representation of independent-particle motion and (b) independent-pair motion. In the first case nucleons (fermions) move independently of each other reflecting elastically from the wall of the mean field created by all the other nucleons, each of which is associated with a Wigner-Seitz cell of volume $(4\pi/3)R_0^3/A = (4\pi/3)r_0^3$, implying a relative distance of $2r_0 (\approx 2.4 \text{ fm})$. Switching on the pairing interaction (bare plus induced) leads to Cooper pair formation in which the correlation length (mean square radius) is ξ . Thus, pair of nucleons moving in time reversal states close to the Fermi energy will tend to recede from each other lowering their relative momentum ($r_0 \rightarrow \xi$) thus boosting the stability of the system, provided that the external mean field allows for it. Or better, if there is nucleon density available to do so, something controlled to a large extent by the single-particle potential. From this point on, and at least for the levels lying close to the Fermi surface, one cannot talk about particles but about Cooper pairs (unless one does not intervene the system with an external field, e.g. (p, d) and provides the energy, angular and linear momentum needed to break a pair). Of course that in the system to the right under the influence of a very strong external field (like e.g. the HF of ^{120}Sn), Cooper pairs will be constrained within its boundaries. But the picture displayed in (b) will be close to be representative in the case of two nuclei of ^{120}Sn at a relative (CM) distance larger than $2R_0 (\approx 12 \text{ fm})$, but still in weak contact. The pair field associated with a Cooper pair will extend from one to the other partner of the heavy ions participating in the reaction through the weakly overlapping interaction region, allowing two nucleons to correlate over a distance ξ and, eventually, in a reaction like e.g. $\text{Sn}+\text{Sn} \rightarrow \text{Sn(gs)}+\text{Sn(gs)}$ allow for the transfer of two nucleons correlated over tens of fm.

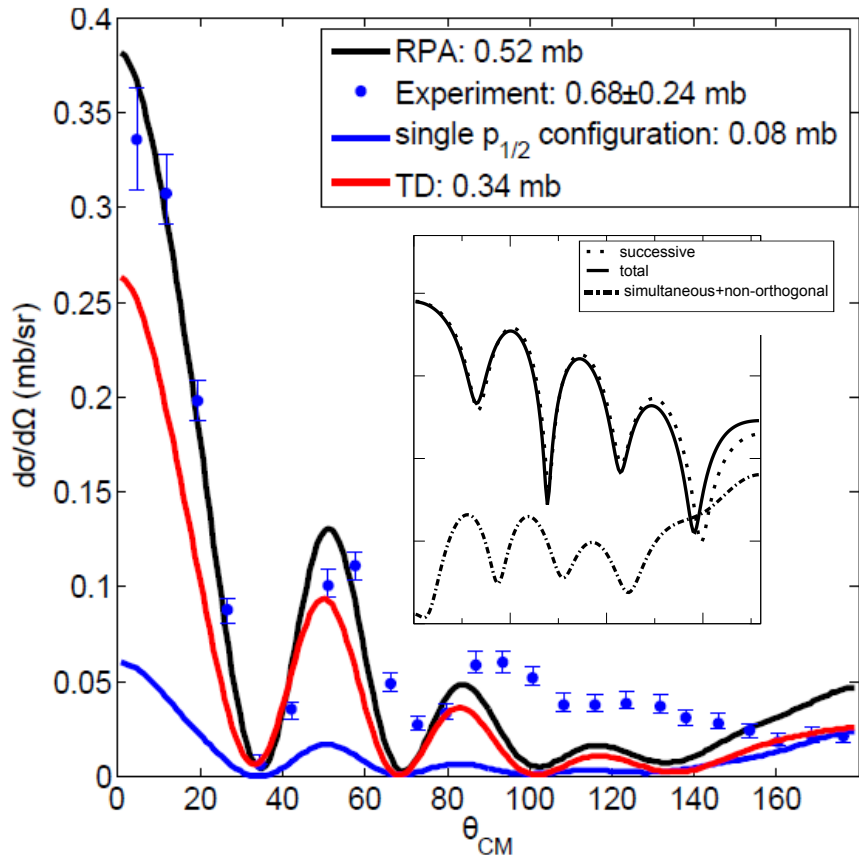


Figure 4.4.4: Absolute two-nucleon transfer differential cross section associated with the $^{206}\text{Pb}(t, p)^{208}\text{Pb}(\text{gs})$ transfer reaction, that is, the annihilation of the pair removal mode of ^{208}Pb in comparison with the data (Bjerregaard, J. H. et al. (1966)). The theoretical cross sections were calculated making use of the spectroscopic amplitudes given in Tables 3.5.2 and 3.5.3 and of global optical parameters as reported in the reference above. Both RPA and TD amplitudes were used as well as a pure configuration $p_{1/2}^2(0)$.

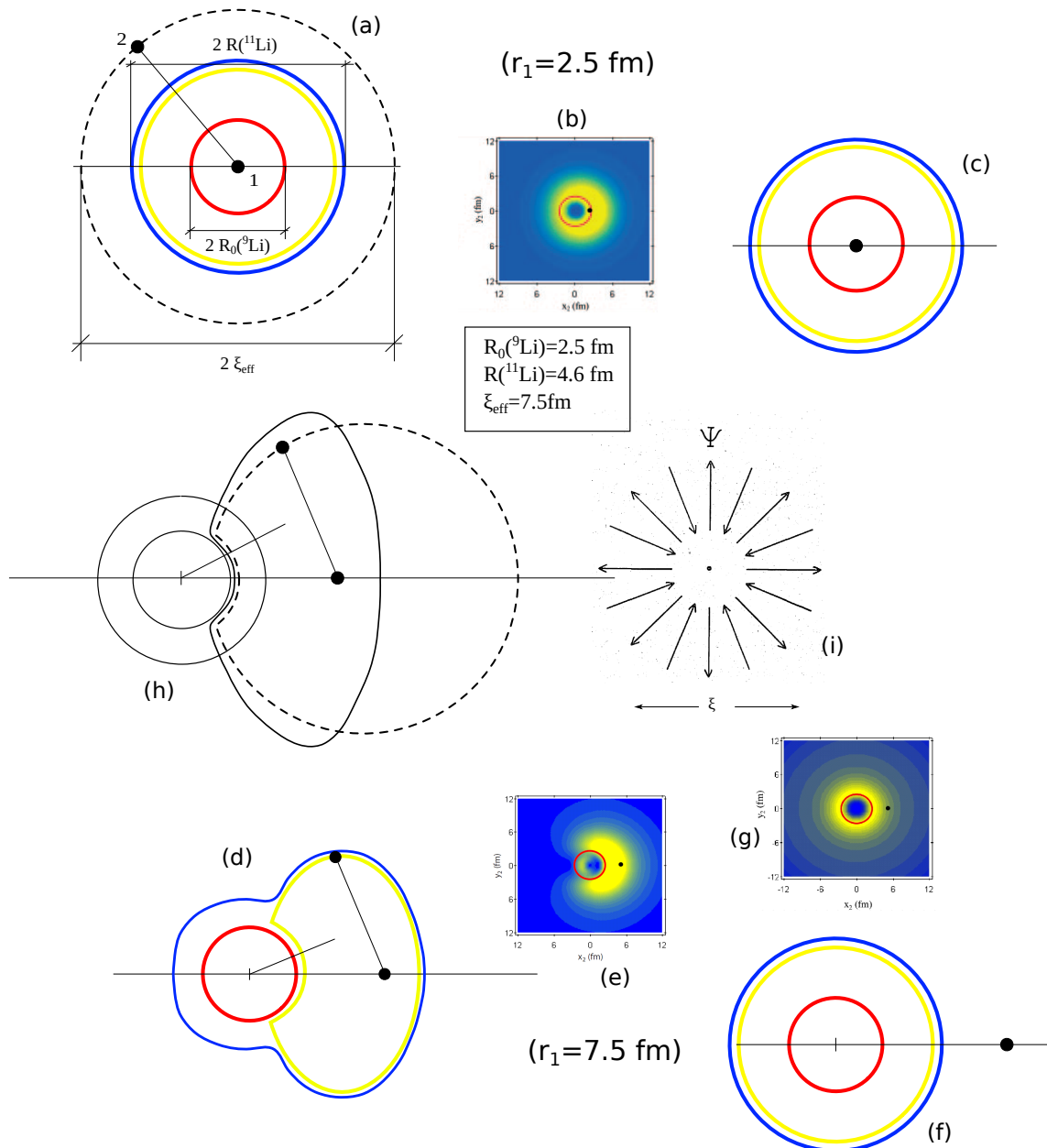


Figure 4.B.1

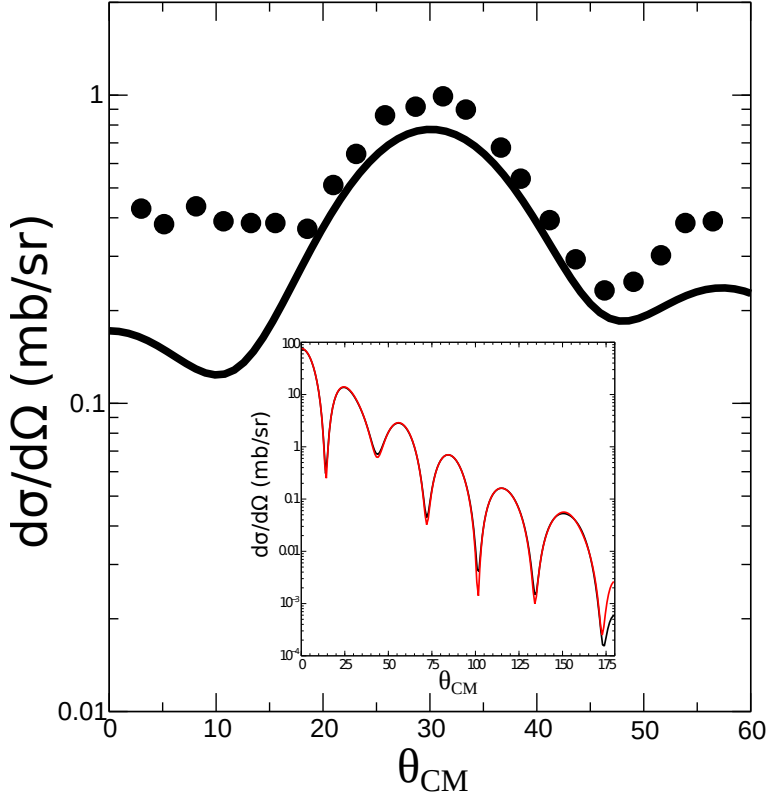


Figure 5.2.1: The absolute differential cross section $^{120}\text{Sn}(p, d)^{119}\text{Sn}(j^\pi)$ associated with the state $j^\pi = 7/2^+$. The theoretical prediction (continuous curve) is displayed in comparison with the experimental data (solid dots, Dickey, S. A. et al. (1982)). The corresponding integrated cross sections are 5.0 and 5.2 ± 0.6 mb respectively. In the inset, and for the sake of accuracy control, the absolute differential cross sections associated with the reaction $^{124}\text{Sn}(p, d)^{123}\text{Sn}(\text{gs})$ calculated making use of the softwares ONE (red) and FRESCO (black (Thompson (1988))) are displayed.

	$^{120}\text{Sn}(p, d)^{119}\text{Sn}$		
	Exp.	Th.	
$j^\pi(lj)$	$E_x(\text{MeV})$	E'_x	\tilde{V}
$7/2^+(g7/2)$	0.788	0.37	0.81

Table 5.2.1: Experimental (E_x) and theoretical (E'_x) quasiparticle excitation energies and theoretical effective occupation probability $\tilde{V}^2 (= 0.66)$ associated with valence orbital $g_{7/2}$ (Idini et al. (2015)).

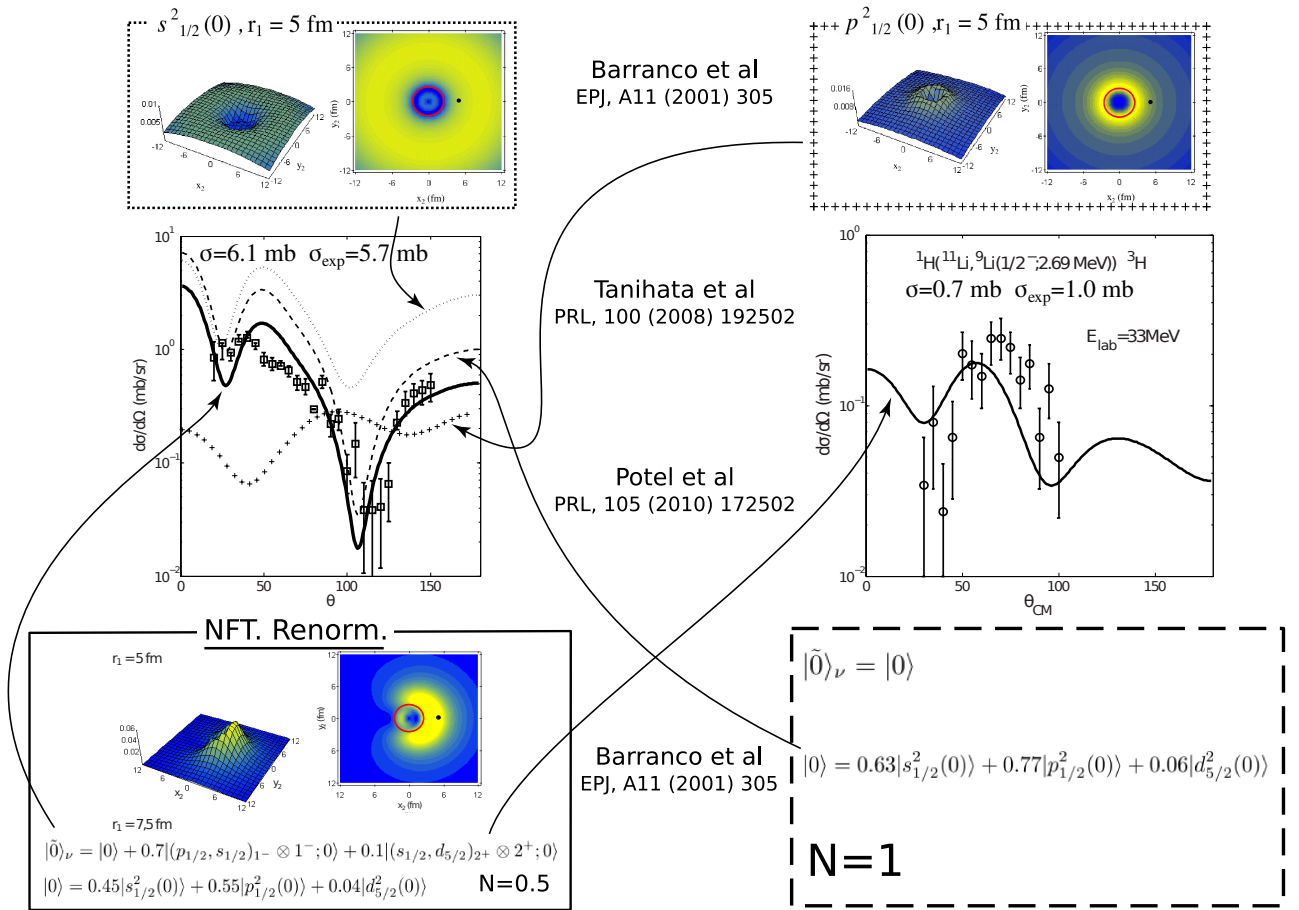


Figure 7.1.3: Absolute, two–nucleon transfer differential cross section associated with the ground state and the first excited state of ${}^9\text{Li}$, excited in the reaction ${}^1\text{H}({}^{11}\text{Li}, {}^9\text{Li}){}^3\text{H}$ (Tanihata, I. et al., 2008) in comparison with the predicted differential cross sections (Potel et al., 2010) worked out making use of spectroscopic amplitudes and Cooper pair wavefunctions calculated with NFT, and of the optical potential collected in Table 7.1.1.

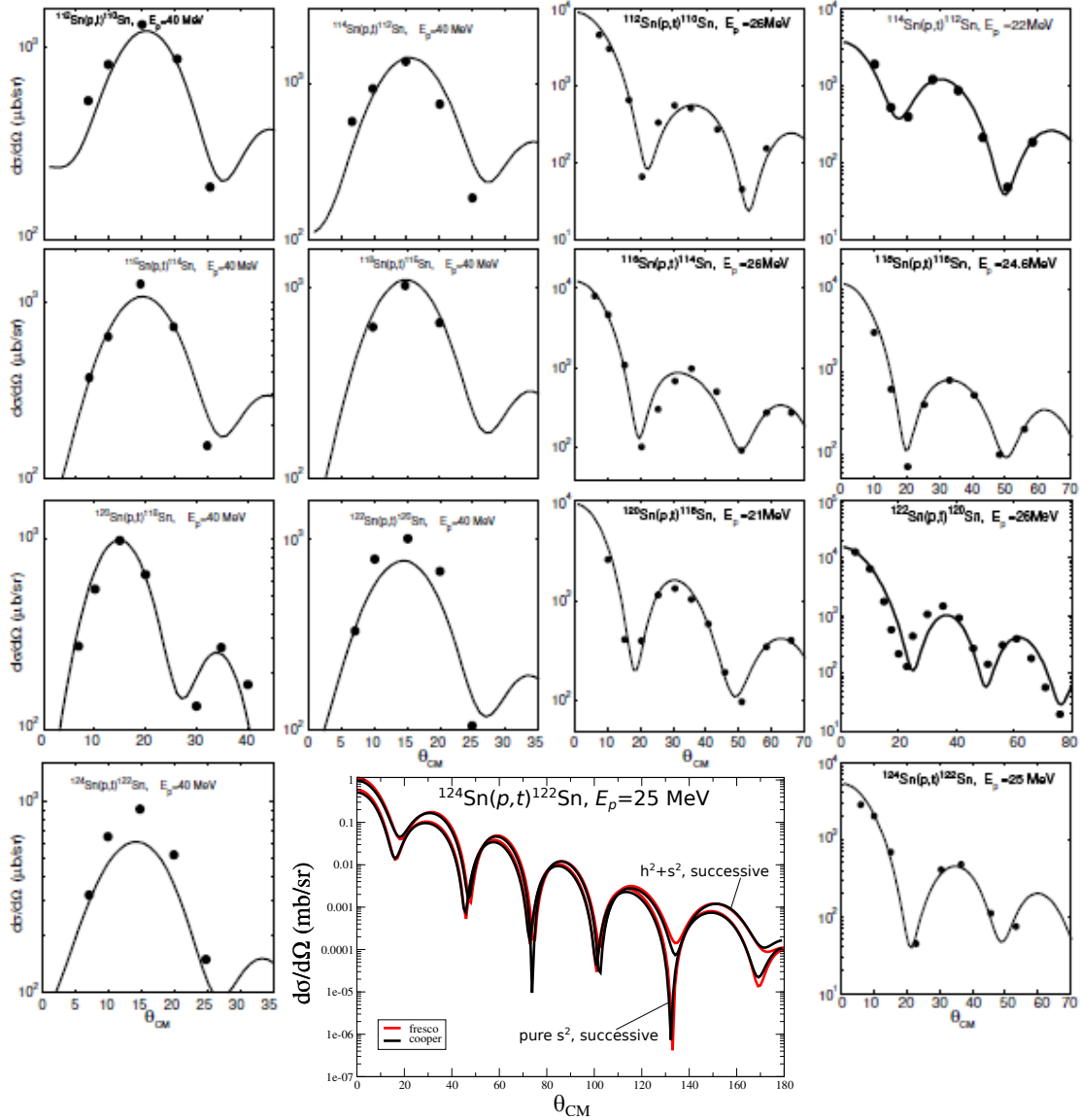


Figure 7.4.1: Predicted (continuous curve, Potel, G. et al. (2013a,b)) absolute differential $^{A+2}\text{Sn} (p, t)^A\text{Sn}(\text{gs})$ cross sections for bombarding energies $E_p=40$ MeV (in the two left columns) and $21 \text{ MeV} \leq E_p \leq 26$ MeV (in the two right columns) in comparison with the experimental data (solid dots, Bassani et al. (1965), Guazzoni, P. et al. (1999), Guazzoni, P. et al. (2004), Guazzoni, P. et al. (2006), Guazzoni, P. et al. (2008), Guazzoni, P. et al. (2011), Guazzoni, P. et al. (2012)). In the center of the lowest row, the absolute differential cross section (successive transfer displayed in the angular interval $0^\circ \leq \theta_{CM} \leq 180^\circ$) associated with the process $^{124}\text{Sn}(p, t)^{122}\text{Sn}(f)$ ($f = h_{11/2}^2(0), s_{1/2}^2(0)$) and calculated with both the software COOPER and FRESCO (Thompson (1988)) are displayed.

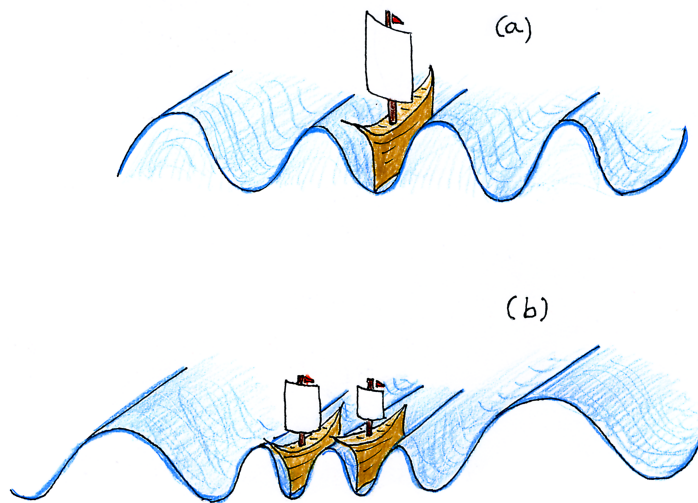


Figure 7.G.2: (Color online) Schematic representation of the behaviour of an isolated ship at sea in a situation of no wind but of strong swell (a), and of two ships close by in similar conditions (b).

At sea, on a windless day in which the water surface can resemble a mirror, free floating ships singly or in groups do not do much, just stay put. The situation is quite different in a strong swell, still on a windless situation. In this case, single, isolated ships end up lying parallel to the wave crests (see Fig. 7.G.2(a)) and start rolling heavily. In the days of the clipper ships it was believed that under those circumstances, two vessels at close distance, attracted each other. This in keeping with the fact that the rigs of the rolling ships became often entangled leading to disaster. It was not until quite recently⁶⁴ that a quantitative understanding of the phenomenon (based on knowledge of similar quantal effects) was achieved, providing evidence that the old tale was true. Only waves with wavelength smaller than the separation of the ships can exist between them. In the region of sea extending away from the ships to the horizon, waves of any wavelength can exist (see Fig. 7.G.2(b)). This fact results into an imbalance between the forces exerted by the internal (between ships) waves, in favour of that exerted by the external waves, leading to a net attraction. Quantum mechanical, such an effect is known as the Casimir effect⁶⁵.

Two conducting, neutral plates at very small distances, of the order of the micron ($1\mu = 10^{-6}$ cm), attract each other, due to the imbalance in electromagnetic field pressure exerted by the bombarding of the surface by electrons and positrons, arising from the ZPF of the electromagnetic field⁶⁶ (see Fig. 7.G.3). It is of no

⁶⁴Boersma (1996).

⁶⁵Casimir (1948).

⁶⁶As stated in the last sentences of the caption to Fig. 7.G.3, long wavelengths play the central

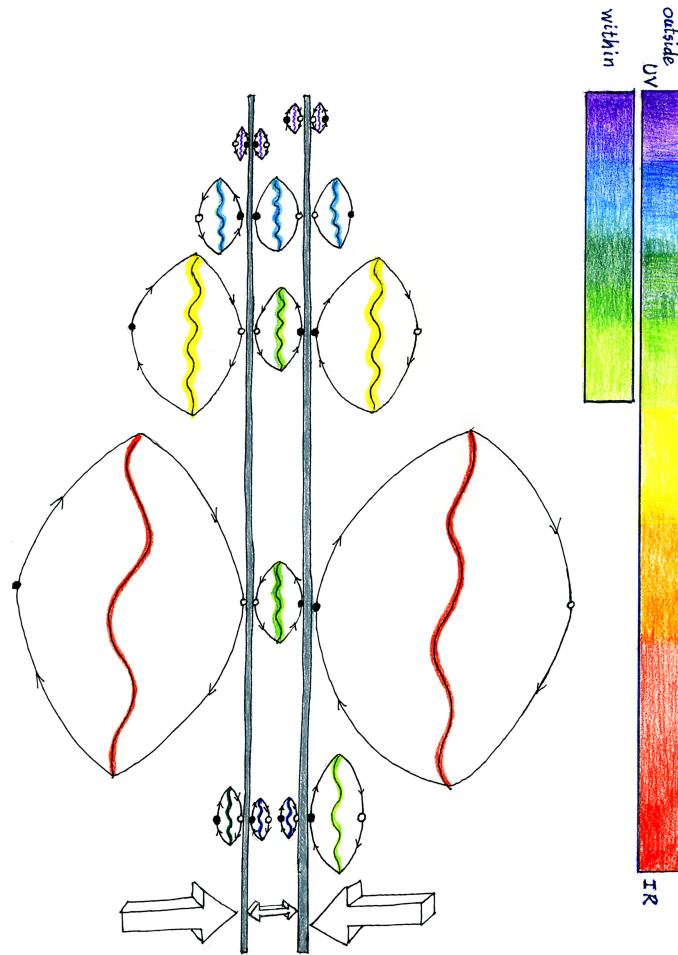


Figure 7.G.3: (Color online) Casimir effect. Two metallic isolated, conducting plates (grey vertical sections) in vacuum attract each other when they are placed at very small distances (of the order of micron). This is known as the Casimir effect. The origin of such a force are, in this work, traced back to quantal zero point fluctuations (ZPF) of the electromagnetic vacuum. In the figure a cartoon of such processes is given. Virtual electrons (e^- , solid dots) and positrons (e^+ , open dots) pop up of the vacuum together with a photon, travel for short distances on timescales of the order of $\hbar/1\text{MeV} \approx 10^{-23}$ s (1 MeV being approximately equal to the summed mass of e^- and e^+). In their way, some of them hit the plates. The different wavelengths of the visible photons (and thus the associate momenta of the fermions), are displayed with the standard color coding of the rainbow. Of course, the spectrum extends beyond such limit (from UV to IR). Because the range of colors (wavelengths) allowed between the plates is smaller than the full spectrum (see colored spectra to the far right of the figure) allowed for the photons associated with the electromagnetic ZPF in the right and left unlimited halves, more fermions or bosons will be knocking the plates from outside than from the in between region, thus leading to an imbalance of the “quantal” pressure and consequently to an effective attractive force. *Within this scenario, there are in fact the long wavelengths of the electromagnetic spectrum which are responsible for the attraction between the metallic plates in the Casimir effect. In other words, quantal pressure by infrared.*

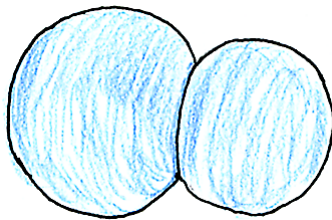


Figure 7.G.4: Two overlapping water droplets attract each other with a potential energy proportional to the surface tension and, making a spherical approximation, as far as the overlapping region is concerned, proportional also to reduced radius or better, to the inverse sum of the curvature. This is also true for two atomic nuclei.

electronic distribution has its charge center closer to the oxygen atom than to the two protons of the H-atoms, H_2O has a sizable dipole moment⁶⁹ ($\approx 0.68ea_0 \approx 0.6$ D, e being the electron charge, a_0 the Bohr radius and D the Debye unit). Water molecules can form four hydrogen bonds⁷⁰ (hb), a special bond between molecules which is produced in situations when they share an hydrogen nucleus between them. The molecule's two hydrogen atoms form two bonds with neighboring oxygens, while the molecule's two lone pairs interact with neighboring hydrogens⁷¹ (Figs. 7.G.5 (b), 7.G.7).

Water and oil do not mix. The term hydrophobic (water-fearing) is commonly used to describe substances that, like oil, do not mix (dissolves) with (in) water. Although it may look as if water repels oil, these two types of molecules actually attract each other, e.g. through the van der Waals interaction, but not nearly as strongly as water attracts itself. Mixing enough oil (hydrophobic, non polar (NP) molecules) with water leads to a reduction in favorable bonding. Strong mutual

⁶⁹The dipole moment of a polar molecule is defined as $u = ql$, where l is the distance between the two charges $+q$ and $-q$. Thus, for two electronic charges $q = \pm e$ separated by $l = 0.1$ nm, the dipole moment is $u = 1.602 \times 10^{-19} \text{ C} \times 10^{-10} \text{ m} = 4.8 \text{ D}$, where the Debye=1D=3.336×10⁻³⁰ Cm is the unit of dipole moment. Small polar molecules have moments of the order of 1D (see e.g. Israelachvili (1985)).

⁷⁰Let us consider an H atom in a covalent bond with oxygen. When a second oxygen atom approaches the H atom, its nucleus, the proton, sees a potential with two minima, and tunnels through the corresponding barrier from one minimum to the other. In other words, the effective potential in which the proton moves becomes broader as compared to the single oxygen potential. Thus, the quantum mechanical confinement kinetic energy decreases by roughly a factor of two. This implies that the order of magnitude energy of an hydrogen bond between two oxygen atoms corresponds to the difference in the corresponding ZPF energies, i.e. ≈ 200 meV ($\approx 0.38 \text{ eV} - 0.19 \text{ eV} \approx 0.2 \text{ eV} \approx 4.6 \text{ kcal/mol}$ ($\approx 8 \text{ kT}$), where kT ($\approx 0.6 \text{ kcal/mol} \approx 27 \text{ meV}$) is the thermal energy at room temperature ($\approx 310 \text{ K}$)). For comparison a covalent bond corresponds to $\approx 96 \text{ kcal/mol} \approx 4 \text{ eV}$, while the van der Waals interaction energy between two H at a distance of 2.4 Å, that is of the order of the hydrogen bond length of 1.83 Å, is ≈ 20 meV (see Povh and Rosina (2002))

⁷¹A possible pedestrian explanation of this is to impersonate a water molecule. Quoting from Ball (2003): “Your hands are hydrogen atoms, your ankles are the lone pairs of electrons of oxygen. Stand legs apart... Twist 90° at the waist, stretch your arms and you’re H_2O . The way that water molecules join up has just one rule: hands can grab ankles, but nothing else. That grasp is an hydrogen bond”.